

# Pressure-Dependent Optical and Vibrational Properties of Monolayer Molybdenum Disulfide

3 Avinash P. Nayak,<sup>†,▲</sup> Tribhuwan Pandey,<sup>‡,▲</sup> Damien Voiry,<sup>§</sup> Jin Liu,<sup>||</sup> Samuel T. Moran,<sup>†</sup> Ankit Sharma,<sup>†</sup>  
 4 Cheng Tan,<sup>†</sup> Chang-Hsiao Chen,<sup>¶</sup> Lain-Jong Li,<sup>○</sup> Manish Chhowalla,<sup>§</sup> Jung-Fu Lin,<sup>||,⊥</sup> Abhishek Singh,<sup>\*,‡</sup>  
 5 and Deji Akinwande<sup>\*,†</sup>

6 <sup>†</sup>Department of Electrical and Computer Engineering, The University of Texas at Austin, Austin, Texas 78712, United States.

7 <sup>‡</sup>Materials Research Center, Indian Institute of Science, Bangalore 560-012, India

8 <sup>§</sup>Department of Materials Science and Engineering, Rutgers University, Piscataway Township, New Jersey 08854, United States

9 <sup>||</sup>Department of Geological Sciences, The University of Texas at Austin, Austin, Texas 78712, United States

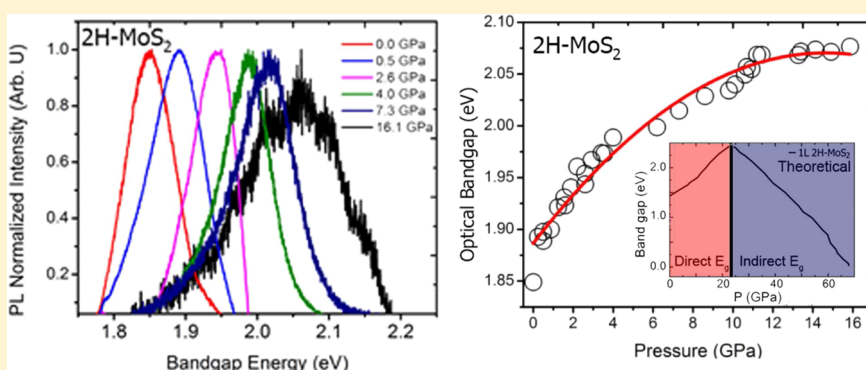
10 <sup>⊥</sup>Center for High Pressure Science and Technology Advanced Research (HPSTAR), Shanghai 201900, China

11 <sup>¶</sup>Institute of Atomic and Molecular Sciences, No. 1, Roosevelt Rd., Sec. 4, Taipei 10617, Taiwan

12 <sup>○</sup>Physical Science and Engineering Division, King Abdullah University of Science & Technology (KAUST), Thuwal 23955, Saudi

13 Arabia

14 Supporting Information



15 **ABSTRACT:** Controlling the band gap by tuning the lattice structure through pressure engineering is a relatively new route for  
 16 tailoring the optoelectronic properties of two-dimensional (2D) materials. Here, we investigate the electronic and lattice  
 17 vibrational dynamics of the distorted monolayer 1T-MoS<sub>2</sub> (1T') and the monolayer 2H-MoS<sub>2</sub> via a diamond anvil cell (DAC)  
 18 and density functional theory (DFT) calculations. The direct optical band gap of the monolayer 2H-MoS<sub>2</sub> increases by 11.7%  
 19 from 1.85 to 2.08 eV, which is the highest reported for a 2D transition metal dichalcogenide (TMD) material. DFT calculations  
 20 reveal a subsequent decrease in the band gap with eventual metallization of the monolayer 2H-MoS<sub>2</sub>, an overall complex  
 21 structure–property relation due to the rich band structure of MoS<sub>2</sub>. Remarkably, the metastable 1T'-MoS<sub>2</sub> metallic state remains  
 22 invariant with pressure, with the J<sub>2</sub>, A<sub>1g</sub>, and E<sub>2g</sub> modes becoming dominant at high pressures. This substantial reversible  
 23 tunability of the electronic and vibrational property of the MoS<sub>2</sub> family can be extended to other 2D TMDs. These results  
 24 present an important advance toward controlling the band structure and optoelectronic properties of monolayer MoS<sub>2</sub> via  
 25 pressure, which has vital implications for enhanced device applications.

26 **KEYWORDS:** 2D Materials, MoS<sub>2</sub>, Transition Metal Dichalcogenide, Strain, Hydrostatic Pressure, Diamond Anvil Cell,  
 27 Pressure Engineering, Photoluminescence

28 Among the great variety of exfoliable materials, transition  
 29 metal dichalcogenides (TMD) have demonstrated prom-  
 30 ising optoelectronic properties. Interestingly, these properties  
 31 can be largely tuned by varying the thickness,<sup>1</sup> by modifying the  
 32 crystal structure,<sup>2</sup> or by applying strain on the TMDs.<sup>3</sup> Pressure  
 33 engineering of the two-dimensional (2D) layered crystals is still  
 34 a relatively new field with many possible routes for further  
 35 investigations and optimization to fully realize their potential in

36 materials engineering.<sup>4–8</sup> Being able to reversibly tune the band  
 37 gap and structure of 2D materials by inducing pressure allows  
 38 for exploring changes in photonic,<sup>9</sup> mechanical,<sup>10</sup> and  
 39 electronic<sup>11</sup> properties at different hydrostatic pressures. The

Received: September 22, 2014

Revised: November 10, 2014

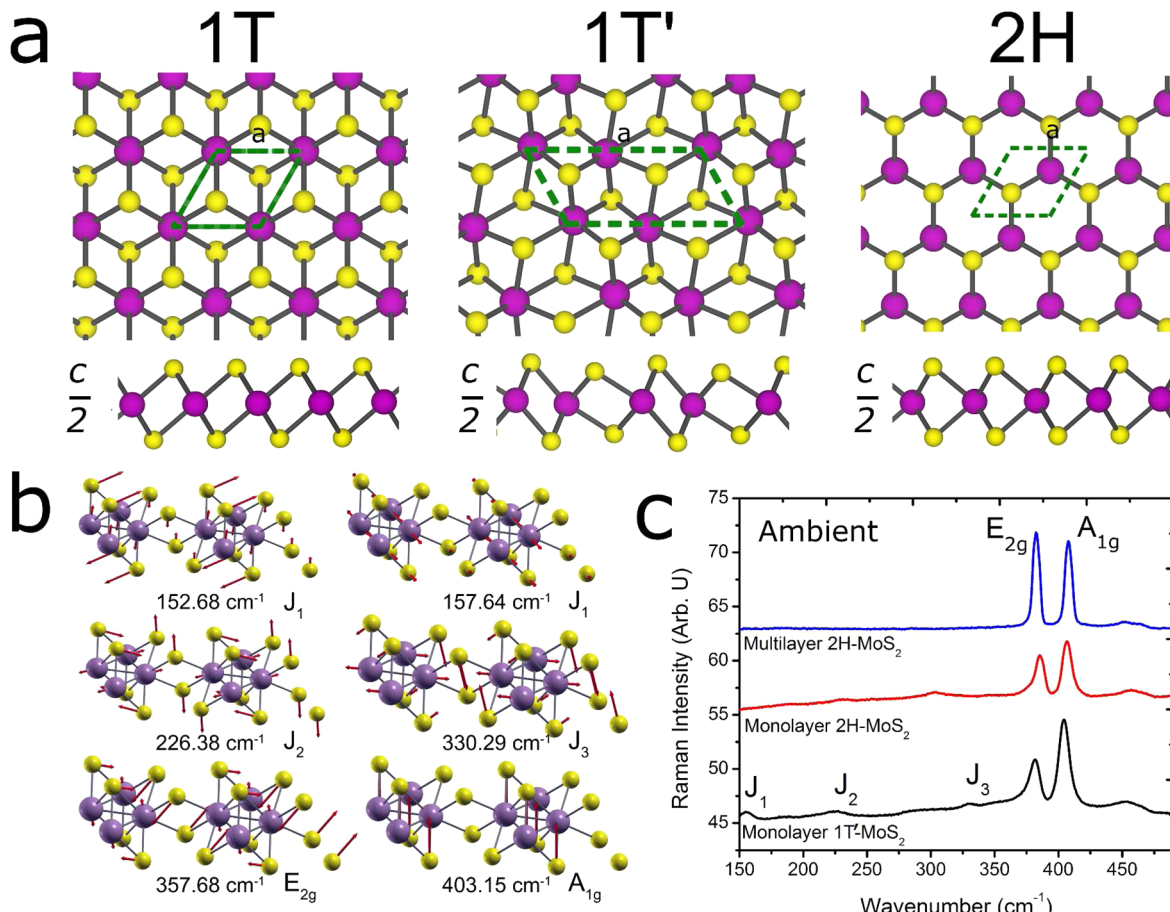


**Figure 1.** Structural and vibrational properties of monolayer MoS<sub>2</sub> polytypes. (a) Schematic atomic arrangements of the monolayer MoS<sub>2</sub> showing the *a* (in-plane direction) and the cross section *c* (out-of-plane) view of the monolayer 1T-MoS<sub>2</sub>, 1T'-MoS<sub>2</sub>, and 2H-MoS<sub>2</sub>. (b) Raman active modes of the MoS<sub>2</sub> family. For the 1T'-MoS<sub>2</sub>, the J<sub>1</sub> mode is composed of two Raman active modes that are close to one another and appear as one peak at room temperature. (c) Raman active modes for the restacked monolayer 1T'-MoS<sub>2</sub> and monolayer and bulk 2H-MoS<sub>2</sub>. The J<sub>1</sub>, J<sub>2</sub>, and J<sub>3</sub> modes are only prominent in the 1T'-MoS<sub>2</sub> phase.

40 effects of hydrostatic pressure on 2D materials are important to  
41 understand, particularly for applications such as flexible  
42 electronics.<sup>5</sup>

43 The transition metal dichalcogenide family, which consists of  
44 2D layered compounds, exhibits a similar laminar structure as  
45 graphene and has been investigated for several optoelec-  
46 tronic<sup>1,12–14</sup> and flexible<sup>5,15</sup> electronics. One representative  
47 TMD that has gained significant interest is molybdenum  
48 disulfide (MoS<sub>2</sub>), which is composed of a single layer of Mo  
49 atoms covalently bonded between two laminar sheets of S  
50 atoms. The natural bulk 2H-MoS<sub>2</sub> is a semiconductor that has  
51 an indirect band gap of 1.3 eV, whereas its monolayer form has  
52 a direct band gap of 1.85 eV due to the lack of interlayer  
53 interactions in thinner layers.<sup>1</sup> Furthermore, depending on the  
54 arrangements of sulfur atoms in the lattice, Mo can be  
55 coordinated either by six sulfur atoms in either an octahedral  
56 (1T), a distorted 1T (1T'), or a trigonal prismatic (2H)  
57 polytype<sup>13</sup> (Figure 1a). This different coordinated structure  
58 also changes the electronic structure of the material. The 1T'-  
59 MoS<sub>2</sub> is metallic, whereas the 2H-MoS<sub>2</sub> is semiconducting.

60 The two main Raman modes in the monolayer 2H-MoS<sub>2</sub> are  
61 the A<sub>1g</sub> and the E<sub>2g</sub> mode. The out-of-plane A<sub>1g</sub> mode occurs  
62 due to opposing vibrations of the two S atoms with respect to  
63 the Mo atom. The E<sub>2g</sub> mode is associated with the in-plane  
64 vibration of the Mo and S atoms, in opposite directions from

one another. For the 1T'-MoS<sub>2</sub>, the experimentally observed J<sub>1</sub>  
65 mode involves two different types of vibrations: one at 152.68  
66 cm<sup>-1</sup>, which is an out-of-plane motion of each stripe of the Mo  
67 atoms inside the zigzag chain, and the other mode at 157.64  
68 cm<sup>-1</sup>, which is an in-plane shearing vibration of one stripe of  
69 atoms with respect to the other atom in the chain. Both of these  
70 modes appear as a single peak at room temperature. The J<sub>2</sub>  
71 peaks at ~226 cm<sup>-1</sup> arises from the motion of two zigzag chains  
72 relative to each other, whereas the mode 330.29 cm<sup>-1</sup>, named  
73 J<sub>3</sub>, tends to break each zigzag chain in two stripes with a slight  
74 out-of-plane component (Figure 1b). Due to the atomic  
75 arrangements of the 1T'-MoS<sub>2</sub> and 2H-MoS<sub>2</sub> phases, these  
76 Raman modes with various magnitudes of activities can be used  
77 to decipher the lattice dynamics of the monolayer polytypes  
78 (Figure 1c).  
79

It has been found experimentally that these two phases can  
80 transition to one another via interlayer atomic plane gliding,  
81 which displaces one of the S planes and changes its electronic  
82 state.<sup>2,13,16</sup> Another way to controllably alter the electronic  
83 properties is to mechanically distort the lattice structure by  
84 applying uniaxial, biaxial, or hydrostatic strain.<sup>17–19</sup> The  
85 majority of research in the field pertains to theoretical  
86 calculations on how the distortion of the 2H and 1T'-MoS<sub>2</sub>  
87 lattice can lead to changes in their photonic and electronic  
88 structure.<sup>12,19–22</sup> Experimentally, it has been a challenge to  
89

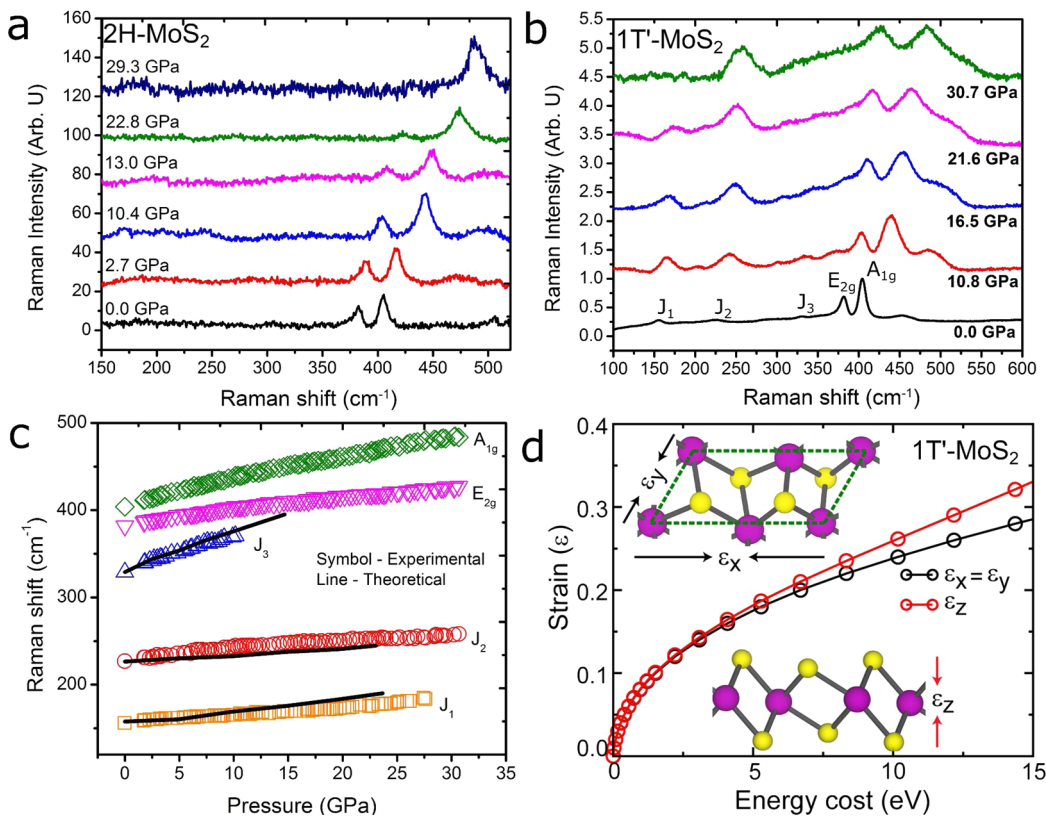


**Figure 2.** Pressure-dependent lattice vibrational properties of monolayer 1T'- and 2H-MoS<sub>2</sub>. Representative Raman spectra of the monolayer (a) 2H-MoS<sub>2</sub> and (b) 1T'-MoS<sub>2</sub> at high pressures. For the 2H-MoS<sub>2</sub> polytype, the E<sub>2g</sub> mode diminishes, whereas the dominant Raman modes are J<sub>2</sub>, E<sub>2g</sub>, and A<sub>1g</sub> for 1T'-MoS<sub>2</sub> at pressures above 27 GPa. (c) Pressure-dependent Raman frequencies with variation in pressure for the five Raman active modes. The J<sub>3</sub> merges with the E<sub>2g</sub> mode at around 10 GPa, whereas the J<sub>1</sub> diminishes at 27 GPa. The solid line indicates the theoretical agreement with the J<sub>1</sub>, J<sub>2</sub>, and J<sub>3</sub> modes and further supports the phonon merging of the J<sub>3</sub> and E<sub>2g</sub> modes. (d) Applied strain is plotted with respect to the energy required to compress the in-plane and out-of-plane bonds, suggesting that the in-plane mode vibration is suppressed at higher pressures. Inset: Schematic representing the application of strain in the in-plane direction ( $\epsilon_x$ ,  $\epsilon_y$ ) (upper inset) and out-of-plane ( $\epsilon_z$ ) directions.

90 exert hydrostatic pressure homogeneously across a 2D sample,  
91 and only a nominal compressive strain of 0.2% or a uniaxial  
92 strain of 10% can be exerted with elaborate setups.<sup>10,11</sup>

93 In the present study, we have investigated the MoS<sub>2</sub> family  
94 (1T'-MoS<sub>2</sub> and both monolayer and bulk 2H-MoS<sub>2</sub>) under  
95 extreme hydrostatic pressures of up to 30 GPa. A diamond anvil  
96 cell (DAC) with a soft neon pressure medium was used to  
97 apply a hydrostatic pressure uniformly across the sample. The  
98 DAC experiments allow fundamental studies of the effects of  
99 high strain levels on the properties of materials, MoS<sub>2</sub> in this  
100 case. This sort of study is important for probing the intrinsic  
101 response of the strain-property relations in a controlled  
102 environment. The insights provided by this study can guide  
103 practical realization of strained MoS<sub>2</sub> devices. The DAC  
104 methodology also permits us to investigate the modulation of  
105 the band gap, the shift from a direct to an indirect band gap,  
106 and the altered phononic properties of both the monolayer 2H-  
107 MoS<sub>2</sub> and 1T'-MoS<sub>2</sub> under applied hydrostatic pressures.  
108 These results show, that for the monolayer 2H-MoS<sub>2</sub> polytype  
109 a ~12% increase in band gap is observed. Although a higher  
110 pressure is not experimentally achievable for the time being, a  
111 metallization at 68 GPa is predicted by theoretical calculations.  
112 The semiconductor to metal transition occurs at a much higher  
113 pressure than that in the bulk counterpart which metallizes at  
114 ~19 GPa. For the 1T'-MoS<sub>2</sub> polytype, the out-of-plane  
115 vibrations are hindered by the hydrostatic pressure, allowing  
116 only the J<sub>2</sub>, A<sub>1g</sub>, and E<sub>2g</sub> vibrational modes to become dominant

at pressures past 27 GPa. Our combined experimental and  
117 theoretical results allow for a coherent understanding of the  
118 vibrational, optical, and electronic properties of TMD materials  
119 as a function of the number of layers and layer geometry under  
120 hydrostatic pressure.  
121

Raman spectroscopy, being fast and nondestructive, is a  
122 powerful diagnostic tool to investigate the vibrational and  
123 physical properties of MoS<sub>2</sub>. Raman spectroscopy has been  
124 used to study 2H-MoS<sub>2</sub> to determine the number of layers,<sup>23</sup> to  
125 determine the effect of pressure on the 2H-MoS<sub>2</sub> lattice,<sup>24–26</sup>  
126 and to determine the level of doping<sup>27</sup> and defects.<sup>28,29</sup> To  
127 understand the electronic and mechanical stability of the MoS<sub>2</sub>  
128 polytypes, we have studied the monolayer and bulk 2H-MoS<sub>2</sub>  
129 as well as restacked monolayer 1T'-MoS<sub>2</sub> under hydrostatic  
130 pressure.  
131

The lattice vibrations detected by Raman spectroscopy can  
132 reveal key changes occurring to the lattice at high pressures. In  
133 particular, hydrostatic pressure can induce a blue shift (phonon  
134 hardening) in MoS<sub>2</sub>.<sup>17</sup> For the 2H-MoS<sub>2</sub> monolayer polytype,  
135 the intensity of in-plane Raman mode (E<sub>2g</sub>) starts to diminish  
136 at pressures above 16 GPa (Figure 2a). The intensity ratio of  
137 A<sub>1g</sub>/E<sub>2g</sub> also increases with pressure (Supporting Information  
138 Figure S1a) above 16 GPa. The diminishing intensity of the E<sub>2g</sub>  
139 mode is attributed to the dominance of normal compressive  
140 strain on the monolayer 2H-MoS<sub>2</sub> under large hydrostatic  
141 pressures,<sup>30</sup> which hinders the in-plane E<sub>2g</sub> movement, whereas  
142

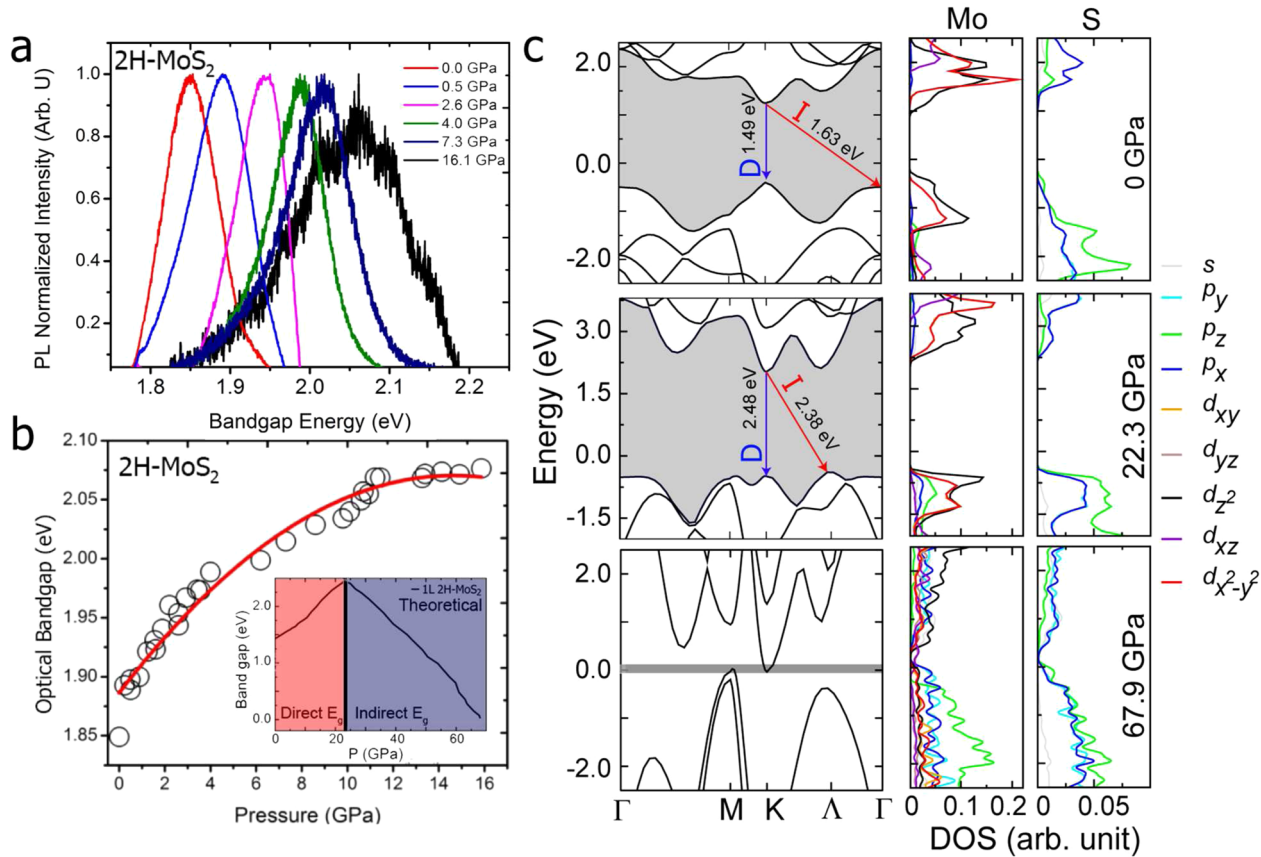


**Figure 3.** Pressure modulated photoluminescent properties of monolayer 2H-MoS<sub>2</sub>. (a) Representative PL spectra as a function of pressure. An increase in the band gap with increasing pressure and then the diminishing of the PL signals at  $\sim 16$  GPa indicates a direct-to-indirect band gap shift. (b) Derived band gap at high pressures. Extracted from the Lorentzian fit from the PL peaks, the band gap is shown to increase as a function of pressure. Red solid line: a polynomial fit to the experimental data described by  $E_g = 1.88 + 0.03P - 8.59 \times 10^{-4}P^2$  where  $E_g$  is optical band gap and  $P$  is pressure. Inset: The theoretical prediction of the direct-to-indirect band gap transition. (c) Band gap diagrams at K,  $\Lambda$ , and  $\Gamma$  point at two representative pressures of 0 and 22.3 GPa depicting the direct to indirect transition. Here, D and I indicate the direct and indirect band gaps, respectively. The observed direct and indirect band gap values are also presented for clarity. At 0 GPa, the  $E-k$  diagram indicates a direct-band gap between the CBM and the VBM, whereas at 22.3 GPa, band gap shift form direct (from in between K-K' points) to indirect in between K- $\Lambda$  points at 22.6 GPa that agrees with the experimental observations. At around 67.9 GPa the valence band maxima (VBM) and the conduction band minima (CBM) cross the Fermi level, leading to a semiconductor-to-metal transition.

143 the A<sub>1g</sub> out-of-plane vibrational mode is still prominent at  
144 pressures up to 30 GPa.

145 Although the rate of increase is higher for A<sub>1g</sub> mode  
146 (Supporting Information Figure S1b), the E<sub>2g</sub> mode also  
147 increases linearly. This distinct rate of increase can be explained  
148 by analyzing the type of vibrations involved in A<sub>1g</sub> and E<sub>2g</sub>  
149 modes. The A<sub>1g</sub> modes originate from transverse vibrations of  
150 S-S atom; however, the E<sub>2g</sub> mode emerges from longitudinal  
151 vibrations of Mo and S atoms in opposite directions. The  
152 change in Mo-S bond length (in-plane movement of atoms)  
153 plays a significant role in determining the behavior of the E<sub>2g</sub>  
154 mode. As the hydrostatic pressure increases, the out-of-plane  
155 (A<sub>1g</sub>) compression becomes more favorable than the in-plane  
156 (E<sub>2g</sub>) compression, indicating that at higher pressures, the  
157 transverse moment of S-S atom is faster than the in-plane  
158 movement of Mo-S atom (Supporting Information Figure  
159 S2a). This results in a higher rate of increase of A<sub>1g</sub> mode with  
160 increasing pressure in comparison to E<sub>2g</sub> mode.

161 Although several studies have been done on the synthesis  
162 and characterization<sup>13,31</sup> of the distorted octahedral 1T'-MoS<sub>2</sub>  
163 polytype, the lattice vibrations at extreme hydrostatic pressure  
164 conditions have not yet been studied under high pressure.  
165 Previous theoretical studies have shown the breaking of lattice

166 symmetry in 1T'-MoS<sub>2</sub> when tensile and compressive strain are applied.<sup>20</sup> The 1T'-MoS<sub>2</sub> phase shows three Raman active  
167 modes that are not present in the trigonal prismatic 2H-MoS<sub>2</sub>  
168 polytype. These three extra modes are the J<sub>1</sub>, J<sub>2</sub>, and J<sub>3</sub>, which  
169 show up at 150 cm<sup>-1</sup>, 225 cm<sup>-1</sup>, and 325 cm<sup>-1</sup>, respectively, at  
170 ambient pressure. As the hydrostatic pressure increases, J<sub>3</sub>  
171 becomes indistinguishable from the E<sub>2g</sub> mode at  $\sim 10$  GPa,  
172 whereas J<sub>1</sub> and J<sub>2</sub> are still prominent at higher pressures. The  
173 broadening of the J<sub>3</sub> mode with pressure further supports the  
174 merging phenomenon of the J<sub>3</sub> and E<sub>2g</sub> modes (Supporting  
175 Information Figure S3). In order to confirm this phonon  
176 merging, theoretical calculations have been carried out to  
177 investigate the effect of pressure on the vibrational properties of  
178 the monolayer 1T'-MoS<sub>2</sub>. The calculated phonon dispersion  
179 curves (Supporting Information Figure S4) at ambient pressure  
180 are consistent with the previously reported results<sup>32</sup> and were  
181 used to identify all the Raman active modes. The theoretically  
182 derived pressure-dependent Raman frequencies show good  
183 qualitative agreement with experimental observation. The  
184 Raman intensity increases for the J<sub>1</sub>, A<sub>1g</sub> and E<sub>2g</sub> modes and  
185 shows the merging of the J<sub>3</sub> and E<sub>2g</sub> modes (Supporting  
186 Information Figure S5). The J<sub>1</sub> Raman mode also diminishes at  
187 pressures above 22 GPa leaving just the J<sub>2</sub>, the A<sub>1g</sub> and the E<sub>2g</sub>  
188

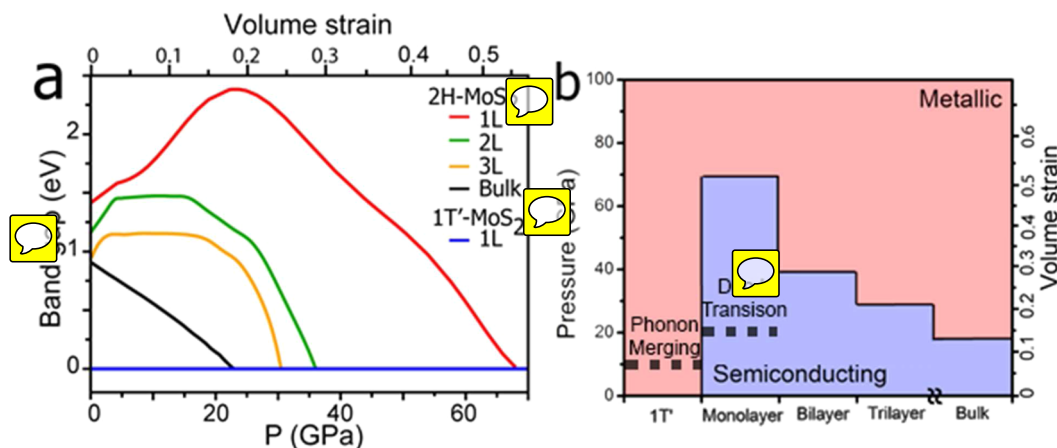


**Figure 4.** Electronic structures of the MoS<sub>2</sub> polytypes under hydrostatic pressure. (a) Band gap energies of the polytypes as a function of pressure. (a) Below 22.3 GPa, an increase in the direct band gap is observed for the monolayer 2H-MoS<sub>2</sub>, whereas for higher pressure, the band gap decreases with strain and closes at 67.9 GPa indicating a metallization transition. A smaller critical pressure of 39.2 and 29.5 GPa is observed for the bilayer and trilayer 2H-MoS<sub>2</sub> respectively. (b) Hydrostatic pressure effects on monolayer, bilayer, trilayer, bulk MoS<sub>2</sub>, and 1T'-MoS<sub>2</sub>. A metallic state is more easily reached in the bulk state because more interlayer interactions are present.

Raman modes dominant at pressures past 27 GPa (Figure 2b). To investigate the E<sub>2g</sub> and J<sub>3</sub> merging in further detail, theoretical calculations were performed to find the dependence on pressure compared to the other modes (Figure 2c). As the hydrostatic pressure increases, the out-of-plane compression becomes favorable (0.08 Å/GPa) than the in-plane compression (0.03 Å/GPa), suggesting that at higher pressures the out-of-plane moment of the S–S atom is faster than the Mo–S movement leading to a smaller rate of increase of the E<sub>2g</sub> mode (1.3 cm<sup>-1</sup>/GPa) compared to the A<sub>1g</sub> mode (2.5 cm<sup>-1</sup>/GPa) (Figure 2d). The pressure-dependent rate of increase for the J<sub>1</sub> and J<sub>2</sub> Raman mode is 0.9 cm<sup>-1</sup>/GPa, whereas the J<sub>3</sub> mode increases at 3.90 cm<sup>-1</sup>/GPa. For the 2H-MoS<sub>2</sub> polytype, the pressure dependence on the Raman modes of the monolayer 2H-MoS<sub>2</sub>, 1T'-MoS<sub>2</sub> and the bulk 2H-MoS<sub>2</sub> shows that the A<sub>1g</sub> and E<sub>2g</sub> modes for both the monolayer 2H-MoS<sub>2</sub> and 1T'-MoS<sub>2</sub> polytypes are similar (Supporting Information Figure S6). For the 2H-MoS<sub>2</sub> monolayer, the shift in Raman peak position increases linearly with applied pressure. The Raman shift with pressure for the A<sub>1g</sub> mode is 2.6 cm<sup>-1</sup>/GPa, whereas the E<sub>2g</sub> mode increases at a rate of 1.7 cm<sup>-1</sup>/GPa (Supporting Information Figure S1b). The distance between A<sub>1g</sub> and E<sub>2g</sub> Raman modes increases at a rate of 1.2 cm<sup>-1</sup>/GPa (Supporting Information Figure S1c). The A<sub>1g</sub> shift for monolayer MoS<sub>2</sub> with pressure, in comparison with other 2D materials such as MoSe<sub>2</sub>, MoTe<sub>2</sub>, and ReS<sub>2</sub>, is higher, signifying that the monolayer MoS<sub>2</sub> has a strong dependence on pressure.<sup>33</sup> The deviation from the bulk MoS<sub>2</sub> is mainly attributed to the interlayer interactions along the out-of-plane axis, which is absent in the monolayer. Unlike the bulk 2H-MoS<sub>2</sub>, no intermediate phase region between the semiconducting and metallic region is observed, indicating that the monolayer MoS<sub>2</sub> does not undergo metallization or a structural transition at pressures up to 30 GPa. Theoretically, we predict the metallization of 2H-MoS<sub>2</sub> to be at ~68 GPa.

Due to the inherent direct band gap (1.85 eV) of the monolayer 2H-MoS<sub>2</sub>, the photonic and electronic band structure can be probed by the photoluminescence (PL) spectroscopy.<sup>29</sup> This strong PL emission is only observed in the monolayer 2H-MoS<sub>2</sub> and is attributed to the slow electronic relaxation that is unique to its electronic structure. The PL

signal for the bilayer and trilayer are much weaker.<sup>29</sup> Our PL spectral measurements on the monolayer 2H-MoS<sub>2</sub> show that the electronic band structure can be significantly modulated by hydrostatic pressure (Figure 3a) at a rate of 30 meV/GPa below 5 GPa. At higher pressures, the direct band gap gradually increases to 2.08 eV at ~12 GPa, showing a significant 11.7% change in band gap (Figure 3b), whereas increasing the PL full width half-maximum (fwhm) (Supporting Information Figure S1d). Although this increase in the direct band gap is reversible (Supporting Information Figure S7), the rate of increase can be altered depending on the pressure medium. This can significantly modify the photonic and electronic characteristics of 2D materials under high pressure.<sup>6,9,34</sup> Because we have used an inert, soft Ne pressure medium in our experiments, our results therefore represent more intrinsic features of the system without dopant effects. The polynomial increase in the band energy is in agreement with theoretical DFT calculations, which show an increase in the direct band gap at the K–K' point. The theoretical band gap is underestimated because the presence of artificial self-interaction and the absence of the derivative discontinuity in the exchange-correlation potential with the PBE/GGA methods.<sup>35</sup> The initial trend in band gap as supported by the PL experiments (Figure 3b) shows an increase at the K–K' point. The in situ fwhm map of PL Spectra (Supporting Information Figure S8) increases from 24.7 nm at 0.6 GPa to 58.7 nm at 12.5 GPa and diminishes to the background noise level at pressures over 16 GPa at room temperature. This increase in the fwhm implies a crossover point to the direct-to-indirect band gap<sup>3</sup> at the K–K' point at approximately 16 GPa. This direct to indirect band gap shift was further confirmed by DFT calculations. The ambient theoretical band gap initially lies in-between K–K' point until a pressure of 22.3 GPa is reached. At 22.3 GPa, a direct-to-indirect transition indicates that the conduction band minima (CBM) and the valence band maxima (VBM) are no longer at the K–K' interband (Figure 3c), but rather shift to the K–Λ point. Theoretical calculations reveal that the band gap of 2H-MoS<sub>2</sub> monolayer first increases up to a pressure of ~22 GPa is reached. Beyond this pressure, the band gap gradually decreases, eventually leading to the metallization of monolayer 2H-MoS<sub>2</sub> at around 68 GPa.

To understand the mechanism for this band gap change and the semiconductor to metal (S–M) transition under hydrostatic pressure, we analyze the contribution from different molecular orbitals by performing angular momentum projected density of states (LDOS) calculations. At lower pressures, both valence (VB) and conduction bands (CB) are mainly composed of Mo- $d_{x^2-y^2}$ ,  $d_z^2$  and S- $p_x$ ,  $p_y$  orbitals (Figure 3c). With increasing pressure, these orbitals move away from the Fermi level, resulting in an increase in band gap up to 22.3 GPa pressure. At higher pressure, the out-of-plane compression becomes more dominant (Supporting Information Figure S2b), which makes the Mo  $d_z^2$ ,  $d_{xz}$ , and  $p_z$  orbitals interact strongly with S  $p_z$  and  $p_x$  orbitals. This strong intralayer hybridization between the orbitals mentioned above leads to a decrease in band gap after ~22 GPa pressure and finally closing of the band gap at higher pressure (68 GPa). For the monolayer 2H-MoS<sub>2</sub>, in-plane intra layer interactions play a dominant role in the metallization at 67.9 GPa.

It was found in our previous study of the bulk MoS<sub>2</sub> that interlayer interactions play a critical role in the metallization.<sup>17</sup> It is therefore expected that as the number of layers increases, the critical pressure or critical volume strain (Supporting Information Figure S10) at which the metallization occurs decreases (Figure 4a). The metallization of the bilayer, trilayer, and bulk 2H-MoS<sub>2</sub> (Figure 4a and b) under high pressure can be understood by the interaction of electron-donating sulfur atoms between the van der Waals gaps.<sup>17,21</sup> The transition pressure for MoS<sub>2</sub> therefore decreases as the number of layers increases. As experimentally observed, the monolayer 1T'-MoS<sub>2</sub> shows metallic behavior (Supporting Information Figure S7), unlike the 2H-MoS<sub>2</sub> polytype which is semiconducting in nature. For the 2H-MoS<sub>2</sub>, the valence and conduction bands are mainly composed of the *d* orbitals of Mo and *p* orbitals of S atoms (Supporting Information Figure S11a). Upon application of hydrostatic pressure the extent of hybridization between Mo *d* orbitals (mainly  $d_z^2$ ,  $d_{xy}$ , and  $d_{x^2-y^2}$ ) and S *p* orbitals increases, thus increasing the overlap between conduction and valence bands resulting in an enhanced metallization (Supporting Information Figure S11b).

We have measured an 11.7% difference in the direct band gap of the 2H-MoS<sub>2</sub> from 1.85 eV at ambient pressure to 2.08 eV at 16 GPa before the PL signal diminished and could no longer be resolved at higher pressures and room temperature. For comparison, a 3.3% difference in direct band gap was found by S.P. Lau et al.,<sup>11</sup> a 3.0% difference by G. A. Steele et al.,<sup>36</sup> and a 5.4% difference by Dou et al.<sup>9</sup> for the monolayer 2H-MoS<sub>2</sub>. To further understand the electronic and phononic properties, DFT calculations were conducted to show that a critical pressure of 67.9 GPa is required to metallize the monolayer 2H-MoS<sub>2</sub>. The 1T'-MoS<sub>2</sub> behaves as a metal at ambient pressure and exhibits three more Raman active modes ( $J_1$ ,  $J_2$ , and  $J_3$ ) in comparison to the 2H-MoS<sub>2</sub>, which exhibits just the  $A_{1g}$  and  $E_{2g}$  modes. At pressures above 10 and 27 GPa, we have observed the diminishing of the out-of-plane  $J_1$  and  $J_3$  Raman modes, respectively, due to higher susceptibility to hydrostatic pressure along the out-of-plane axis. At 10 GPa, the  $J_3$  mode starts to merge with the  $E_{2g}$  mode. The suppression of the  $J_1$  mode at ~27 GPa is attributed to the large hydrostatic pressure on the lattice implying that the effect of pressure is more pronounced for this mode and is more sensitive to pressure. Because this process is reversible for both the 2H-MoS<sub>2</sub> and the 1T'-MoS<sub>2</sub>, the distortion of the lattice is predicted to be a transitory structural modification. The total

energy calculation also reveals that monolayer MoS<sub>2</sub> is the most stable phase under the applied pressure range (Supporting Information Figure S12), and confirms that there is no phase transformation between 2H and 1T' phase within the studied range of pressure.

Strain engineering of 2D layered materials is a relatively new field with possible routes for further investigations to fully realize their potential in customizing material behavior. Here, the interplay of the structural and optoelectronic properties is successfully described for the MoS<sub>2</sub> family. The monolayer 2H-MoS<sub>2</sub> differs from its bulk counterpart because the bandgap increases by ~12% with applied hydrostatic pressure due to the absence of interlayer interactions. For the intrinsically metallic 1T'-MoS<sub>2</sub>, interlayer structural distortion is prevalent resulting in phonon merging of two Raman active modes ( $J_1$  and  $E_{2g}$ ) at high pressures. The large reversible bandgap modulation of semiconducting MoS<sub>2</sub> is attractive for highly tunable optoelectronics, nanoelectronics, and flexible electronics and can enable new opportunities based on the dynamic strong electron–phonon coupling.

**Experimental Methods.** *Sample Preparation.* The 2H-MoS<sub>2</sub> monolayer were synthesized based on our previous work.<sup>37</sup> In brief, 300 nm SiO<sub>2</sub> substrates were placed in the center of a tubular furnace. Precursors of 0.3 g MoO<sub>3</sub> (Sigma-Aldrich, 99.5%) in Al<sub>2</sub>O<sub>3</sub> crucible was placed 12 cm away from substrates and S (Sigma-Aldrich, 99.5%) powder in quartz tube was evaporated in tube and reacted with Al<sub>2</sub>O<sub>3</sub>. The furnace was first heated to 150 °C at 10 °C/min rate with 70 sccm Ar at 10 Torr and annealed for 20 min, then reached 650 °C at 25 °C/min rate and kept for 1 h. After growth, furnace was slowly cooled to room temperature. The as-grown MoS<sub>2</sub> film was broken into thin pieces that were used after cleaning the substrate with acetone. The thinned down sample was transferred over to the DAC by a 10 μm edged tweezer and was studied as is.

1T'-MoS<sub>2</sub> samples were synthesized by Li intercalation using *n*-butyllithium as explained elsewhere.<sup>13</sup> The Li<sub>x</sub>MoS<sub>2</sub> was retrieved by filtration and washed with hexane (60 mL) to remove excess *n*-butyllithium and other organic residues. Exfoliation was achieved by ultrasonication Li<sub>x</sub>MoS<sub>2</sub> in water at a concentration of 1 mg/mL for 1 h. The mixture was centrifuged several times to remove lithium cations in the form of LiOH as well as nonexfoliated materials.

**Characterization.** For the Raman spectroscopic studies on the 2H and 1T' polytypes, a green 532 nm Coherent Verdi V2 laser was used at the Mineral Physics Laboratory of the University of Texas at Austin. The scattered light was dispersed by an 1800 grooves/mm grating and collected by an EMCCD (Andor Technology) resulting in a spectral resolution of approximately 1 cm<sup>-1</sup>. To avoid potential overheating or oxidizing of the samples, the highest laser power level used was 20 mW with a focused laser beam size of 10 μm. Ruby fluorescence spectra were also collected using the same system for pressure calibrations<sup>38</sup> (Supporting Information Figure S8).

For the photoluminescence (PL) and Raman in situ mapping studies on the 2H-MoS<sub>2</sub>, a grating of 900 grooves/mm was used. A long working-distance (LD EC) objective, Epiplan-Neofluar (20×/0.22 DIC M27), was used. The Witec Alpha 300 micro-Raman confocal microscope with a 488 nm laser was used for the in situ PL and Raman mapping studies. To better understand the band gap energy of the system, a Lorentzian curve fit to the PL curves was used to derive the peak energy positions as well as the band widths.<sup>39</sup>

**Theoretical Calculations. Modeling of Hydrostatic Pressure on Monolayer MoS<sub>2</sub>.** The hydrostatic pressure on the monolayer was modeled by calculating the ease of compression along the *x*, *y*, and *z* direction. First, we checked the individual energy costs for in-plane (*x*, *y*) and out of plane (*z*). Based on the energy cost calculation we calculated the compression along all directions for hydrostatic pressure modeling (Supporting Information Figure S2a and S2b). A similar procedure was followed for 1T'-MoS<sub>2</sub> monolayer.

For 2, 3L, and bulk MoS<sub>2</sub>, first we approximate the in-plane (change in *a*, *b*) and out-of-plane (change in slab thickness *c*) compression by performing total energy calculation. First, we apply a uniform strain in all direction calculate the energy cost. By comparing the energy cost for biaxial and normal compressive strain, we extract the atomic displacement. Due to presence of weak van der Waals (vdW) interaction in between the layers the slab thickens decreases more rapidly in comparison to in plane lattice parameter *a* and *b* as shown in Supporting Information Figure S13 (a) for 2L MoS<sub>2</sub>.

In order to correlate the theoretical finding with experiments, it is important to estimate applied hydrostatic pressure. The applied pressure was calculated from the energy cost per unit volume as per the following equation for 1L, 2L, 3L, and bulk MoS<sub>2</sub>

$$P = \frac{E - E_0}{V - V_0}$$

where, *E* (*E*<sub>0</sub>) and *V* (*V*<sub>0</sub>) are the energy and volume for the unstrained (strained) systems. The volume of a hexagonal lattice can be defined as *V* = *a*<sup>2</sup> *c* sin (60°) where *a* is the in-plane lattice parameter and *c* is thickness of slab. The thickness of various structures is defined as shown in Supporting Information Figure S13. As shown in our previous work,<sup>17</sup> the theoretical calculated pressure agrees well with the experimental pressure for bulk MoS<sub>2</sub>.

**First-Principles Theoretical Calculations.** Theoretical calculations were performed using first-principle ab initio density functional theory (DFT) using Vienna Ab Initio Simulation Package (VASP).<sup>40</sup> All-electron projector augmented wave potentials<sup>41,42</sup> and the Perdew–Burke–Ernzerhof<sup>43</sup> generalized gradient approximation (GGA) were used to account for the electronic exchange and correlation. The structure of the 1T'-MoS<sub>2</sub> monolayer is generated by following the approach of Calandra.<sup>23</sup> All the structures were relaxed in the *x*-*y* plane while constraining the *z* coordinates by employing a conjugate gradient scheme until the forces on every atom were minimized to be less than 0.005 eV/Å. A well-converged Monkhorst–Pack *k* point set of 15 × 15 × 1 was used for this procedure. The phonon dispersion of monolayer MoS<sub>2</sub> was calculated using density functional perturbation theory (DFPT)<sup>44</sup> as implemented in VASP. An additional tool, Phonopy,<sup>45</sup> which supports the VASP interface, was used for extracting the phonon frequencies. The force constants were calculated with a supercell of 2 × 2 × 1 and the *k* point set of 13 × 13 × 1. In order to obtain accurate phonon frequencies, a high energy cutoff of 600 eV and strict energy convergence criterion of 10<sup>-11</sup> eV were used.

## ASSOCIATED CONTENT

### Supporting Information

Here, you will find further experimental and theoretical support for the optical and structural properties discussed in this manuscript. This material is available free of charge via the Internet at <http://pubs.acs.org>.

## AUTHOR INFORMATION

### Corresponding Authors

\*E-mail: dej@ece.utexas.edu.

\*E-mail: abhishek@mrc.iisc.ernet.in.

### Author Contributions

▲The manuscript was written through contributions of all authors. All authors have given approval to the final version of the manuscript. These authors contributed equally.

### Notes

The authors declare no competing financial interest.

## ACKNOWLEDGMENTS

Research at The University of Texas at Austin was supported by a Young Investigator Award (D.A.) from the Defense Threat Reduction Agency (DTRA), the Army Research Office (ARO), and the Southwest Academy of Nanoelectronics (SWAN) center sponsored by the Semiconductor Research Corporation (SRC). Research at Indian Institute of Science was supported by National Program on Micro and Smart Systems (NpMASS) PARC No. 1:22 and DST Nanomission. We would like to thank Megan Matheney for providing critical feedback. J.F.L. acknowledges supports from Energy Frontier Research in Extreme Environments (EFree), Center for High Pressure Science and Advanced Technology (HPSTAR), and the U.S. National Science Foundation Geophysics Program. L.J.L. acknowledges support from Academia Sinica Taiwan and KAUST, Saudi Arabia.

## REFERENCES

- (1) Mak, K. F.; Lee, C.; Hone, J.; Shan, J.; Heinz, T. F. *Phys. Rev. Lett.* **2010**, *105* (13), 136805.
- (2) Chhowalla, M.; Shin, H. S.; Eda, G.; Li, L.-J.; Loh, K. P.; Zhang, H. *Nat. Chem.* **2013**, *5* (4), 263–275.
- (3) Conley, H. J.; Wang, B.; Ziegler, J. I.; Haglund, R. F.; Pantelides, S. T.; Bolotin, K. I. *Nano Lett.* **2013**, *13* (8), 3626–3630.
- (4) Artyukhov, V. I.; Liu, M.; Yakobson, B. I. *Nano Lett.* **2014**, *14* (8), 4224–4229.
- (5) Chang, H.-Y.; Yang, S.; Lee, J.; Tao, L.; Hwang, W.-S.; Jena, D.; Lu, N.; Akinwande, D. *ACS Nano* **2013**, *7* (6), 5446–5452.
- (6) Proctor, J. E.; Gregoryanz, E.; Novoselov, K. S.; Lotya, M.; Coleman, J. N.; Halsall, M. P. *Phys. Rev. B* **2009**, *80* (7), 073408.
- (7) Restrepo, O. D.; Mishra, R.; Goldberger, J. E.; Windl, W. *J. Appl. Phys.* **2014**, *115* (3), 033711–033711–8.
- (8) Frank, O.; Tsoukleri, G.; Riaz, I.; Papagelis, K.; Parthenios, J.; Ferrari, A. C.; Geim, A. K.; Novoselov, K. S.; Gallois, C. *Nat. Commun.* **2011**, *2*, 255.
- (9) Dou, X.; Ding, K.; Jiang, D.; Sun, B. *ACS Nano* **2014**, *8* (7), 7458–7464.
- (10) Pérez Garza, H. H.; Kievit, E. W.; Schneider, G. F.; Staufer, U. *Nano Lett.* **2014**, *14* (7), 4107–4113.
- (11) Hui, Y. Y.; Liu, X.; Jie, W.; Chan, N. Y.; Hao, J.; Hsu, Y.-T.; Li, L.-J.; Guo, W.; Lau, S. P. *ACS Nano* **2013**, *7* (8), 7126–7131.
- (12) Najmaei, S.; Zou, X.; Er, D.; Li, J.; Jin, Z.; Gao, W.; Zhang, Q.; Park, S.; Ge, L.; Lei, S.; Kono, J.; Shenoy, V. B.; Yakobson, B. I.; George, A.; Ajayan, P. M.; Lou, J. *Nano Lett.* **2014**, *14* (3), 1354–1361.
- (13) Eda, G.; Yamaguchi, H.; Voiry, D.; Fujita, T.; Chen, M.; Chhowalla, M. *Nano Lett.* **2011**, *11* (12), 5111–5116.

- s13 (14) Ganatra, R.; Zhang, Q. *ACS Nano* **2014**, *8* (5), 4074–4099.  
s14 (15) Lee, J.; Tao, L.; Parrish, K. N.; Hao, Y.; Ruoff, R. S.; Akinwande,  
s15 D. *Appl. Phys. Lett.* **2012**, *101* (25), 252109–2–252109–4.  
s16 (16) Duerloo, K.-A. N.; Li, Y.; Reed, E. J. *Nat. Commun.* **2014**, *5*, 1–  
s17 9.  
s18 (17) Nayak, A. P.; Bhattacharyya, S.; Zhu, J.; Liu, J.; Wu, X.; Pandey,  
s19 T.; Jin, C.; Singh, A. K.; Akinwande, D.; Lin, J.-F. *Nat. Commun.* **2014**,  
s20 *5*, 1–9.  
s21 (18) Bissett, M. A.; Tsuji, M.; Ago, H. *Phys. Chem. Chem. Phys.* **2014**,  
s22 *16* (23), 11124–11138.  
s23 (19) Guo, H.; Lu, N.; Wang, L.; Wu, X.; Zeng, X. C. *J. Phys. Chem. C*  
s24 **2014**, *118* (13), 7242–7249.  
s25 (20) Hu, T.; Li, R.; Dong, J. *J. Chem. Phys.* **2013**, *139* (17),  
s26 1747022–1747027.  
s27 (21) Bhattacharyya, S.; Singh, A. K. *Phys. Rev. B* **2012**, *86* (7),  
s28 075454.  
s29 (22) Espejo, C.; Rangel, T.; Romero, A. H.; Gonze, X.; Rignanese, G.  
s30 M. *Phys. Rev. B* **2013**, *87* (24), 245114.  
s31 (23) Terrones, H.; Corro, E. D.; Feng, S.; Poumirol, J. M.; Rhodes,  
s32 D.; Smirnov, D.; Pradhan, N. R.; Lin, Z.; Nguyen, M. A. T.; Elias, A.  
s33 L.; Mallouk, T. E.; Balicas, L.; Pimenta, M. A.; Terrones, M. *Sci. Rep.*  
s34 **2014**, *4*, 1–9.  
s35 (24) Sugai, S.; Ueda, T. *Phys. Rev. B* **1982**, *26* (12), 6554–6558.  
s36 (25) Aksoy, R.; Selvi, E.; Ma, Y. *J. Phys. Chem. Solids* **2008**, *69* (9),  
s37 2138–2140.  
s38 (26) Chi, Z.-H.; Zhao, X.-M.; Zhang, H.; Goncharov, A. F.; Lobanov,  
s39 S. S.; Kagayama, T.; Sakata, M.; Chen, X.-J. *Phys. Rev. Lett.* **2014**, *113*  
s40 (3), 036802.  
s41 (27) Sercombe, D.; Schwarz, S.; Pozo-Zamudio, O. D.; Liu, F.;  
s42 Robinson, B. J.; Chekhovich, E. A.; Tartakovskii, I. I.; Kolosov, O.;  
s43 Tartakovskii, A. I. *Sci. Rep.* **2013**, *3*, 1–6.  
s44 (28) Ling, X.; Fang, W.; Lee, Y.-H.; Araujo, P. T.; Zhang, X.;  
s45 Rodriguez-Nieva, J. F.; Lin, Y.; Zhang, J.; Kong, J.; Dresselhaus, M. S.  
s46 *Nano Lett.* **2014**, *14* (6), 3033–3040.  
s47 (29) Li, H.; Zhang, Q.; Yap, C. C. R.; Tay, B. K.; Edwin, T. H. T.;  
s48 Olivier, A.; Baillargeat, D. *Adv. Funct. Mater.* **2012**, *22* (7), 1385–1390.  
s49 (30) Bandaru, N.; Kumar, R. S.; Sneed, D.; Tschauner, O.; Baker, J.;  
s50 Antonio, D.; Luo, S.-N.; Hartmann, T.; Zhao, Y.; Venkat, R. *J. Phys.*  
s51 *Chem. C* **2014**, *118* (6), 3230–3235.  
s52 (31) Jiménez Sandoval, S.; Yang, D.; Frindt, R. F.; Irwin, J. C. *Phys.*  
s53 *Rev. B* **1991**, *44* (8), 3955–3962.  
s54 (32) Calandra, M. *Phys. Rev. B* **2013**, *88* (24), 245428.  
s55 (33) Tongay, S.; Sahin, H.; Ko, C.; Luce, A.; Fan, W.; Liu, K.; Zhou,  
s56 J.; Huang, Y.-S.; Ho, C.-H.; Yan, J.; Ogletree, D. F.; Aloni, S.; Ji, J.; Li,  
s57 S.; Li, J.; Peeters, F. M.; Wu, J. *Nat. Commun.* **2014**, *5*, 1–6.  
s58 (34) Nicolle, J.; Machon, D.; Poncharal, P.; Pierre-Louis, O.; San-  
s59 Miguel, A. *Nano Lett.* **2011**, *11* (9), 3564–3568.  
s60 (35) Perdew, J. P.; Zunger, A. *Phys. Rev. B* **1981**, *23* (10), 5048–  
s61 5079.  
s62 (36) Castellanos-Gomez, A.; Roldán, R.; Cappelluti, E.; Buscema, M.;  
s63 Guinea, F.; van der Zant, H. S. J.; Steele, G. A. *Nano Lett.* **2013**, *13*  
s64 (11), 5361–5366.  
s65 (37) Lee, Y.-H.; Zhang, X.-Q.; Zhang, W.; Chang, M.-T.; Lin, C.-T.;  
s66 Chang, K.-D.; Yu, Y.-C.; Wang, J. T.-W.; Chang, C.-S.; Li, L.-J.; Lin, T.-  
s67 W. *Adv. Mater.* **2012**, *24* (17), 2320–2325.  
s68 (38) Mao, H. K.; Xu, J.; Bell, P. M. J. *Geophys. Res.: Solid Earth* **1986**,  
s69 *91* (B5), 4673–4676.  
s70 (39) Buscema, M.; Steele, G.; van der Zant, H. J.; Castellanos-  
s71 Gomez, A. *Nano Res.* **2014**, *7* (4), 1–11.  
s72 (40) Kresse, G.; Hafner, J. *Phys. Rev. B* **1993**, *47* (1), 558–561.  
s73 (41) Kresse, G.; Joubert, D. *Phys. Rev. B* **1999**, *59* (3), 1758–1775.  
s74 (42) Blöchl, P. E. *Phys. Rev. B* **1994**, *50* (24), 17953–17979.  
s75 (43) Perdew, J. P.; Burke, K.; Ernzerhof, M. *Phys. Rev. Lett.* **1996**, *77*  
s76 (18), 3865–3868.  
s77 (44) Gonze, X.; Lee, C. *Phys. Rev. B* **1997**, *55* (16), 10355–10368.  
s78 (45) Togo, A.; Oba, F.; Tanaka, I. *Phys. Rev. B* **2008**, *78* (13),  
s79 134106.